

On the Computational Entanglement of Distant Features in Adversarial Machine Learning

YenLung Lai, XingBo Dong, and Zhe Jin

Abstract—Adversarial examples in machine learning has emerged as a focal point of research due to their remarkable ability to deceive models with seemingly inconspicuous input perturbations, potentially resulting in severe consequences. In this study, we undertake a thorough investigation into the emergence of adversarial examples, a phenomenon that can, in principle, manifest in a wide range of machine learning models. Through our research, we unveil a new notion termed computational entanglement, with its ability to entangle distant features, display perfect correlations or anti-correlations regardless to their spatial separation, significantly contributes to the emergence of adversarial examples. We illustrate how computational entanglement aligns with relativistic effects such as time dilation and length contraction to feature pair, ultimately resulting in the convergence of their angle differences and distances towards zero, signifying perfect correlation, or towards maximum, indicating perfect anti-correlation.

Index Terms—Computational Entanglement, Adversarial Machine Learning, Special Relativity, Information Reconciliation



1 INTRODUCTION

Adversarial Example introduce a noteworthy attribute, which is the ability to deceive disparate machine learning models despite differences in their architectures or training datasets. Through meticulous manipulation of input images, attackers can create adversarial examples that remain imperceptibly altered to the human eye, thereby presenting considerable challenges in detection and raising awareness of their potentially adverse implications [1]. Furthermore, when these different models are deceived by an adversarial example, they tend to agree with each other on the incorrect class prediction. This transferability phenomenon challenges the conventional belief that models with varying characteristics would possess diverse vulnerabilities and make dissimilar errors [2]. It also implies the existence of common vulnerabilities or analogous decision boundaries across diverse models. Despite their differences, these models may possess susceptibility to similar input perturbations or exhibit similar decision-making mechanisms that are sensitive to adversarial manipulations. The transferability of adversarial examples raises concerns about the robustness and generalizability of machine learning models, whereby an attacker is able to train their own substitute model, generate adversarial examples against the substitute, and successfully exploit the vulnerabilities of a victim model with minimal knowledge about it.

In the rapidly evolving machine learning landscape, various techniques for crafting less human-perceptible adversarial examples have arisen, including spatial transformations proposed by Xiao et al. [3], the application of generative adversarial networks showcased by Baluja and Fischer [4], Xiao et al. [5], and Hossain et al. [6], and the

recent diffusion model-based approach introduced by Chen et al. [7].

Extensive research has been conducted to investigate the transferability phenomenon, and numerous theories have emerged to explain its underlying mechanics. These theories commonly posit that adversarial examples occur due to complex and high dimensional inconsistencies present in the training data [8]–[10]. Nevertheless, these theories have yet to provide a complete understanding that succinctly portrays how this phenomenon operates in practical settings.

1.1 Non-Robust Features vs Bugs Debate

Despite the incomplete understanding of adversarial transferability’s root cause, the drive to maximize machine learning model accuracy has shown no signs of slowing down [11], [12]. This belief in accuracy improvement as a means to enhance adversarial robustness is unyielding.

Ilyas et al. [13] emphasized this in their work, suggesting that human-understandable explanations closely tied to model training are essential. They introduced a fresh perspective, arguing that adversarial examples stem from a model’s sensitivity to non-robust features with strong generalization properties, not anomalies. They suggests a nuanced understanding of non-robust features in models, arguing that they are not inherently “useless”. Rather, their functionality resides in regions that might not align with human intuition or contemplation. Such features are essential when the ultimate goal is achieving the highest possible accuracy.

Nakkiran [14] conducted experiments using projected stochastic gradient descent (PGD) demonstrate the ability to control how well adversarial examples deceive different models by managing information leakage. These findings suggest that adversarial examples can result from factors beyond non-robust features, including how information is harnessed and how models are trained. They further conducted another experiment to illustrate that adversarial

YenLung Lai, XingBo Dong, and Zhe Jin are with Anhui Provincial Key Laboratory of Secure Artificial Intelligence; Anhui Provincial International Joint Research Center for Advanced Technology in Medical Imaging, School of AI, Anhui University, Hefei 230093, China. (e-mail: {yenlung, xingbo.dong, jinzhe}.ahu.edu.cn)

examples can indeed be also “just bugs,” emerging due to factors like limited data samples, overfitting, and labeling errors.

While Wallace’s [15] challenge to Ilyas’ findings suggested that model distillation might have played a role, where information from one model influenced another due to incorrect labels in adversarial examples initially derived from a correctly labeled dataset, Ilyas maintained that this doesn’t undermine their central claim. According to Ilyas, the only features that could have been transferred through distillation were the non-robust ones, thereby upholding the core of their argument.

Overall, despite the ongoing debate sparked by Ilyas et al. [13], the notion of non-robust features has widely influenced subsequent works, laying the groundwork for further exploration [16]–[21].

One notable development is the emergence of a new perspective that considers physics: adversarial examples can be viewed as artifacts, neither purely features nor bugs, resulting from interactions between systems and the real world. Buckner [18] illustrates this concept using the Doppler effect as an example, demonstrating how artifacts can be misleading, such as changes in sound or light frequency due to the motion of objects.

1.2 Adversarial Linearity Hypothesis

While exploring non-robust features may enhance predictions and control in machine learning, there’s a challenge: *can humans truly grasp these complex non-robust features intuitively?* Striking a balance between exploring them and keeping scientific explanations comprehensible and interpretable to human understanding is crucial.

Goodfellow et al., [2] have considered contemporary neural networks, despite their intricate architecture, are inherently piecewise linear preceding the final sigmoid or softmax layer. These networks effectively partition the input space into distinct linear subregions, maintaining linearity within each of these regions regarding input responses. They argue that adversarial examples, intriguingly, emerge from the network’s capacity for linearly extrapolating pixel values to extremes. This insight is substantiated by the network’s logit values, which demonstrate a linear response when subjected to various levels of adversarial noise.

Subsequently, Moosavi et al. [22] have observed that training models on adversarial examples (to reduce vulnerability to such examples) results in the network behaving in a more linear manner. They frame adversarial training as an effective means of regularizing the curvature of the model’s decision boundaries. Notably, Moosavi et al. acknowledge that their results contradict Goodfellow et al.’s perspective, but they do not propose alternative explanations to counter the evidence supporting linearity as a significant factor.

Tanay and Griffin [23] challenged Goodfellow et al.’s linear interpretation of adversarial examples, indicating its lack of persuasiveness or completeness. They argued that in specific linear classification scenarios exemplified by two distinct image classes, i.e. black and white, adversarial examples are absent. This absence stems from the precise feature representation learned by the linear Support Vector Machine (SVM) model. The SVM effectively disregards

noise in one image half while accurately recognizing distinguishing features in the other half, establishing a clear and well-defined decision boundary between the classes. They highlighted that the current linear interpretation failed to predict which learned feature classes would be affected to induce adversarial effects. They further defined “adversarial strength” as a measure to quantify the impact of adversarial examples; and demonstrated that this measure is intricately linked to the angle deviation between the weight vector of the considered classifier and the weight vector of the nearest centroid classifier.

Shamir et al. [24] posited that this phenomenon originates from the inherent geometry of \mathbb{R}^n using the Hamming metric. They perceive this implication as extremely counterintuitive and enigmatic, suggesting that all piece-wise linear neural network-defined classes are interconnected in a fractal-like structure. Expanding upon this profound insight, Shamir et al. [25] introduced the dimpled manifold model. This model encapsulates the neural network training process by dynamically adjusting the network’s decision boundary within a low-dimensional image manifold using the techniques of “clinging” and “dimpling.” Adversarial examples are conceptualized as pseudo images positioned both “below” and “above” this manifold.

While the cause of adversarial examples is still under debate, Goodfellow et al.’s linear interpretation (explained in [26]) clarifies why simpler models like shallow radial basis function (RBF) networks exhibit greater resilience to adversarial attacks compared to neural networks. This interpretation also uncovers an intriguing observation: various linear models demonstrate similar responses to the same adversarial example, even after training on distinct datasets. It provides valuable insights into model interpretability, outlier resilience, and underscores the significance of comprehending adversarial examples within the larger scope of machine learning models.

Summary of Results: In this work, we delve into the underlying reasons for the emergence of adversarial examples in contemporary machine learning. We’ve developed a physical model to simulate adversaries’ ability to independently construct machine learning models using available physical resources via parameter inferencing.

Our model deeply rooted in physical laws, particularly the second law of thermodynamics, which posits an ever-increasing system entropy. We introduce new notion of *computational entanglement* which enables the establishment of strong correlations between distant features. A more in-depth analysis uncovers intriguing connections between our model and Einstein’s theory of special relativity. Through iterative feature encoding, computational entanglement causes distinct features, regardless of their spatial separation, to become entangled. This entanglement correlation which is computational in nature, emerge from the effect of time dilation and length contraction, leading to the convergence of their angle difference, normalized Hamming and Euclidean distances, to zero.

We showcase the generation of adversarial examples through information reconciliation within linear models, driven by computational entanglement. This implies that adversarial examples indeed can be viewed as a unique manifestation of information reconciliation, where human

imperceptible, entangled noise is incorporated into images. These findings align with the linearity hypothesis put forth by Goodfellow et al. [2], suggesting that all piecewise linear models are susceptible to computational entanglement effects; At least, in principle, we have demonstrated that there *exist* an efficient linear encoding function capable of entangling distinct features, possibly leading to misclassifications.

In addition, we’ve observed a noteworthy aspect: the computational entanglement correlations exhibit two distinct behaviors, converging in both opposite directions. This means that by altering the sign of the input feature samples, these entangled features shift from perfect correlation to perfect anti-correlation, i.e., their, angle differences, Hamming distance (after normalized), and Euclidean distance can be either zero or maximum. This observation sheds light on the potential for boundary conditions to change simply by reversing the sign of input features. What a model initially struggled to classify can eventually be correctly classified due to this reversal. This highlights the model’s sensitivity to slight changes in input and its potential to transition from vulnerability to robustness with a simple sign reversal.

2 ADVERSARIAL LEARNING MODEL

We begin with the definition of an adversarial learning model, which is characterized by parameter inference, a vital yet longstanding concept in machine learning, without making additional assumption over the computational power of the adversary. More specific, it follows the Bayesian inference (a.k.a Bayes’s Theorem) that combines prior beliefs of arbitrary random distribution \mathcal{D} with observed data $x \in \mathcal{D}$, to offer precise uncertainty measures for achieving model objective.

Adversary Model’s Objective: By means of parameter inference, the objective of the defined model is to identify a parameter value, denoted as θ_0 , that maximize the posterior probability $P(\theta_0 = \theta|\mathcal{D})$, given an arbitrary random distribution, denoted as \mathcal{D} . We here consider the true parameter, denoted as θ_0 , to be unknown; if it were otherwise, there would be no problem to resolve. The primary objective is to maximize the likelihood of an inferred parameter, θ , being identical to the true parameter θ_0 . Using Bayes’ Theorem, it can be formally described as:

$$P(\theta = \theta_0|\mathcal{D}) = \frac{P(\mathcal{D}|\theta = \theta_0) \cdot P(\theta = \theta_0)}{P(\mathcal{D})} \quad (1)$$

In above equation, $P(\mathcal{D}|\theta = \theta_0)$ represents the “likelihood” of the distribution \mathcal{D} given the inferred parameter θ . The term $P(\theta = \theta_0)$, known as the “prior”, reflects our initial belief concerning the value of θ prior to any data observation. The denominator $P(\mathcal{D})$, or the “evidence”, serves as a normalizing constant which ensures the probabilistic coherence of the equation. Disregarding the denominator could lead to the right-hand side of the equation failing to constitute a probability, thereby not necessarily falling between 0 and 1.

In the following paragraph, we demonstrate that the adversary model’s objective can be achieved through maximizing the likelihood, which ultimately represents the binary entropy of the true parameter θ_0 .

Likelihood Maximization: Given any training sample $x \in \mathcal{D}$, we can identify an explicit function f within \mathcal{F} , which maps the sample statistic to θ , that is $\theta = f(x_1, \dots, x_N)$ holds true for all x within \mathcal{D} . However, if this is not achievable, we should resort to numerical optimization. In this case, we choose the parameter value of θ that maximizes the likelihood of the data in order to fulfil our objective. In a conventional machine learning model, the process of maximization can be represented as follows:

$$\hat{\theta} = \arg \max_{\theta} \mathcal{L}(\theta; \mathcal{D}),$$

where $\hat{\theta}$ is our inferred parameter, and the likelihood typically referred to as joint density of $x \in \mathcal{D}$ that described as a function of θ expressed as:

$$\begin{aligned} \mathcal{L}(\theta; \mathcal{D} = x_1, \dots, \mathcal{D} = x_N) &= f(\mathcal{D} = x_1, \dots, \mathcal{D} = x_N; \theta_1, \dots, \theta_N) \\ &= \prod_{i=1}^N f(\mathcal{D} = x_i; \theta_i) = \prod_{i=1}^N f(\mathcal{D} = x_i; \theta). \end{aligned} \quad (2)$$

The last line follows a common assumption used in machine learning that all training samples $(x_1, \dots, x_N) \in \mathcal{D}$ are independent and identically distributed (i.i.d).

Notably, the maximization of the likelihood can be done by minimizing the “negative log likelihood”, that is:

$$-\frac{1}{N} \log \mathcal{L}(\theta; \mathcal{D}) = -\frac{1}{N} \sum_{i=1}^N \log(f(\mathcal{D} = x_i; \theta)), \quad (3)$$

where we take the average via dividing the likelihood by $1/N$.

Directly solving the minimization problem as stated above would not provide a meaningful result because it does not give us any information about the true distribution of \mathcal{D} . The true distribution should correspond to the true parameter θ_0 . Therefore, we employ a mathematical strategy of adding zero to the above equation, i.e., adding and subtracting the log-likelihood of $\log(f(\mathcal{D} = x_i; \theta_0))$. Consequently, bringing the negative term inside, we yield the following expression:

$$\frac{1}{N} \left[\sum_{i=1}^N \log \left(\frac{f(\mathcal{D} = x_i; \theta_0)}{f(\mathcal{D} = x_i; \theta)} \right) - \sum_{i=1}^N \log(f(\mathcal{D} = x_i; \theta_0)) \right] \quad (4)$$

For all $x \in \mathcal{D}$, with sufficiently large N , Eq. 4 converges (in quadratic mean) to its expected value, result to:

$$D_{KL}(f(x; \theta_0) || f(x; \theta)) + H(f(x; \theta_0)) \quad (5)$$

where

$$\begin{aligned} H(f(x; \theta_0)) &= -\mathbb{E}[\log(f(x; \theta_0))] \\ &= -\int_{\mathbb{R}} f(x; \theta_0) \log(f(x; \theta_0)) dx \end{aligned}$$

is the differential entropy of the true density $f(x; \theta_0)$ (according to the asymptotic equipartition theorem) and

$$D_{KL}(f(x; \theta_0) || f(x; \theta)) = \int_{\mathbb{R}} f(x; \theta_0) \log \left(\frac{f(x; \theta_0)}{f(x; \theta)} \right) dx$$

is the Kullback-Leibler (KL) divergence, i.e., relative entropy between the true density ($f(x; \theta_0)$) and the parameter-inferred density ($f(x; \theta)$), which is a positive term and equal to zero only if $\theta = \theta_0$.

The optimal goal for the adversary is to attain $\theta = \theta_0$, where this leads us to the average minimum negative log likelihood equivalent to

$$-\frac{1}{N} \log \mathcal{L}(\theta; \mathcal{D}) = H(f(x; \theta_0)). \quad (6)$$

Challenges with Non-Determinism in Standard Approaches: Noting that above defined adversary learning model is of information theoretic, applicable to any machine learning model aiming to minimize the loss function or maximize likelihood. Yet, achieving $\theta = \theta_0$ in practice can be challenging due to factors like model complexity and noise, resulting in non-zero Kullback-Leibler divergence. Most importantly, the entropy of the likelihood function described above is non-deterministic, and cannot be further reduced without precise knowledge of the density function $f(\cdot)$. This would involve setting its derivative with respect to θ_0 to zero. For this outlined reason, we discern a theoretical constraint imposed by conventional optimization strategies in minimizing the negative log likelihood function. The non-deterministic nature of this scenario introduces an element of uncertainty, prompting us to consider an alternative approach: employing coding approach [27] that involves transforming feature samples into higher-dimensional codewords; with the aim of ensuring the model’s correctness and completeness in the inference of arbitrary parameters $\theta_1, \theta_2, \dots, \theta_t$.

3 MODEL’S CORRECTNESS AND COMPLETENESS

We begin by formalizing the model’s “correctness,” which refers to model’s confidence in predicting outcomes correctly or generating “good” adversarial examples. It provides insight into the likelihood of accurately inferring a parameter, ensuring that $\theta = \theta_0$ holds across various random inputs. As we will demonstrate in the forthcoming sections, the computational efficiency of our model serves as a testament to its practical adversarial implications for real-world machine learning models, even when confronted with stringent deterministic requirement of $\theta = \theta_0$.

3.1 Model’s Correctness

In our context, we redefine non-robust features, as those with low real-world occurrence probabilities. This definition is intuitive because rare or infrequent features can be challenging for humans to recognize across various domains. Our reformulation emphasizes that a feature’s robustness depends on the model’s capability to detect its presence and understand its impact. This consideration, particularly relevant for adversarial examples, is vital for improving a model’s ability to effectively learn from and predict such features.

3.1.1 A Physical Model Designation Based on Second Law of Thermodynamics and Computational Entanglement

We adopt a coding methodology, which view a pair of feature samples, denoted as $w \in \mathbb{R}^k$ (and $w' \in \mathbb{R}^k$), as analogous to a corresponding pair of ‘messages’, each with a dimension of k . This ‘message’ pair undergoes a transformation into its respective pair of codewords (typically inhabits a larger-dimension $n > k$), represented as $c \in \mathbb{R}^n$ (and

$c' \in \mathbb{R}^n$). A smaller distance between codewords suggests a stronger correlation (i.e., intraclass) between their original features, while a larger distance implies a weaker correlation (i.e., interclass) between their original features.

To align with the discrete notion of conventional coding approaches [27], we denote $x = d_H(c, c')$, as the Hamming distance between the codewords post quantization. The term ‘quantization’ refers to quantizing the codeword values by their sign into the set $\{-1, 1\}$, creating n -dimensional binary vectors for c and c' where

$$\Pr[x = k] = \theta^k (1 - \theta)^{n-k}. \quad (7)$$

The annotation in Eq. 7 narrows our attention to those distributions that can be described with the inferred parameter θ , with codewords distance equal to k . This annotation is crucial as it describes arbitrary codewords distance $x \in \mathcal{D}$ as an i.i.d Bernoulli variable characterized by θ .

While that is common for standard machine learning models to assume that training data is i.i.d without additional constrain; However, this assumption can be quite idealistic which often doesn’t hold in practical applications. Users might introduce manipulated data that violates this i.i.d assumption [28] potentially allow transferability of adversarial examples across different models [29].

In the context of the aforementioned, we can describe the parameter-inferred density $f(x; \theta)$ corresponds to the inferred parameter (θ) as a function of (x, k, θ) follows:

$$f(x; \theta) \Rightarrow f(x, k; \theta) = \Pr[x = k] = \theta^k (1 - \theta)^{n-k}.$$

Given above description, it becomes logical to define the true density, which corresponds to θ_0 , as conforming to a Binomial distribution:

$$f(x; \theta_0) \Rightarrow f(x, k; \theta_0) = \binom{n}{k} \theta_0^k (1 - \theta_0)^{n-k}.$$

The reason for this formulation is to establish a rigorous relationship between the parameter-inferred density density and the true density function. This relationship can be written as follows:

$$\frac{f(x, k; \theta_0)}{f(x, k; \theta)} = \binom{n}{k} \quad (8)$$

if and only if $\theta = \theta_0$.

Above description only cater relationship between a single true parameter, θ_0 , and a single inferred parameter, θ . For the sake of model completeness (will be elaborated in Section 3.2), we consider the possibility of using a finite number of parameters to describe the true densities of the system, i.e., $\theta_0, \theta_1, \dots, \theta_{t+1}$, expressed as:

$$\begin{aligned} & \frac{f_0(x, k; \theta_0) f_1(x, k; \theta_1) \dots f_{t-1}(x, k; \theta_{t-1}) f_t(x, k; \theta_t)}{f_0(x, k; \theta_1) f_1(x, k; \theta_2) \dots f_{t-1}(x, k; \theta_t) f_t(x, k; \theta_{t+1})} \\ &= \left(\frac{\binom{n}{k} \theta_0^k (1 - \theta_0)^{n-k}}{\theta_1^k (1 - \theta_1)^{n-k}} \right) \left(\frac{\binom{n}{k} \theta_1^k (1 - \theta_1)^{n-k}}{\theta_2^k (1 - \theta_2)^{n-k}} \right) \dots \\ & \left(\frac{\binom{n}{k} \theta_{t-1}^k (1 - \theta_{t-1})^{n-k}}{\theta_t^k (1 - \theta_t)^{n-k}} \right) \left(\frac{\binom{n}{k} \theta_t^k (1 - \theta_t)^{n-k}}{\theta_{t+1}^k (1 - \theta_{t+1})^{n-k}} \right) \\ &= \prod_{i=0}^t \frac{f_i(x, k; \theta_i)}{f_i(x, k; \theta_{i+1})} = \binom{n}{k}^{t+1} \left(\frac{\theta_0^k (1 - \theta_0)^{n-k}}{\theta_{t+1}^k (1 - \theta_{t+1})^{n-k}} \right), \quad (9) \end{aligned}$$

if and only if $\theta_0 = \theta_1 = \dots = \theta_{t+1}$.

Our formalization significantly diverges from conventional machine learning models. In our approach, the inferred parameter with density $f(x, k; \theta)$ is an unique instance of the true density, following a Binomial distribution, and is allowed to evolve, transitioning from a single case to $\binom{n}{k}$ possible cases. This ongoing process leads to an exponentially increasing constant, which we refer to as the ‘‘entanglement complexity’’. This constant encompasses all $t + 1$ parameters $(\theta_0, \dots, \theta_{t+1})$ that characterize the evolving system’s true densities over time. We conveniently designate t as the ‘‘encoding time step.’’ An increase in t correlates with longer computation time, indicative of heightened computational complexity.

To gain more insight into the described entanglement effect, we explore the rationale behind formalizing densities corresponding to the same parameter. This transition, from $f_0(x, k, \theta_1)$ to $f_1(x, k, \theta_1)$ -from single state to multi-states, aligns with the principles of the *second law of thermodynamics*, indicating a tendency toward increased entropy within isolated systems until equilibrium is reached. However, even in equilibrium, the system’s evolution does not necessarily cease, drawing inspiration from the work of Brown and Susskind [30]. We, therefore, formalize the system’s ongoing evolution, considering its susceptibility to disturbances such as entanglement.

In this study, we computationally liken entanglement to an encoding process capturing the system’s dynamically evolving states, such as the density transition from $f_1(x, k, \theta_1)$ to $f_1(x, k, \theta_2)$ -from multi-states back to single state. These operations adhere to the *principle of conservation of information*, preserving the system’s order and information completeness. This preservation allows the system to represent original states and their progression, resulting in entropy reduction.

Following encoding, another density transition occurs, from $f_2(x, k, \theta_2)$ to $f_3(x, k, \theta_2)$, guided by the same underlying law, resulting in entropy increase. Suppose there is only single parameter θ to consider. By substituting Eq. 8 into Eq. 4, we obtain the following result:

$$\begin{aligned} & \frac{1}{N} \sum_{i=1}^N \left[\log \binom{n}{k} - \log \left(\binom{n}{k} \theta_0^k (1 - \theta_0)^{n-k} \right) \right] \\ & = -\log((\theta_0)^k (1 - \theta_0)^{n-k}). \end{aligned}$$

The result derived above substantiates the proposition that the minimization problem, previously delineated in Eq. 3, can indeed be effectively reduced to the minimization of the negative log-likelihood of a specific Binomial distribution. In this context, the solution for θ_0 that maximize the likelihood can be determined by differentiating the negative logarithm of the aforementioned likelihood function with respect to θ_0 and setting the resultant value to zero. This approach leads us to the following:

$$\begin{aligned} & \frac{d(-\log((\theta_0)^k (1 - \theta_0)^{n-k}))}{d\theta_0} = 0 \\ & \Rightarrow \left(\frac{\theta_0}{1 - \theta_0} - \frac{k}{n - k} \right) \Rightarrow \theta_0 = \frac{k}{n}, \end{aligned}$$

with $\theta_0 = k/n$ maximizes the likelihood function. This give us the *deterministic* solution of average minimum negative log likelihood described as:

$$-\frac{1}{N} \log \mathcal{L}(\theta; \mathcal{D}) = nH_2(\theta_0) = nH_2(k/n) \quad (10)$$

where $H_2(\cdot)$ denotes the binary entropy function.

3.1.2 Explicit Model Construction

To explicitly construct the aforementioned model, we leverage the concept of Locality Sensitive Hashing (LSH) for encoding, to generate codewords that follow a Binomial distribution from arbitrary pairs of random feature samples.

Encoding via Cosine Distance-based LSH [31]: Given two random feature samples $w_t \in \mathbb{R}^k$ and $w'_t \in \mathbb{R}^k$, start from $t = 0$, which can be normalized to vectors have unit norm. The Cosine Distance-based LSH defines individual functions $h_i(\cdot)$ using a randomly chosen normal unit vector $v_i \in \mathbb{R}^k$. This is expressed as

$$h_i(w_0) = (v_i^T \cdot w_0) \in \mathbb{R}, \text{ for } i = 1, \dots, n.$$

To ensure the independence of the functions $h_i(\cdot)$, it is crucial to draw their projection vectors v_i independently from the standard normal distribution with a mean of zero and a variance of one. Let’s formally define a generator function G_t . This function comprises a set of hash functions h_1, \dots, h_n .

When we apply cosine distance-based LSH, the resulting output vector is referred to as an n -dimensional codeword. This codeword incorporates all $h_i \in G_t$:

$$\begin{aligned} c_0 &= G_0(w_0) = (h_1(w_0), \dots, h_n(w_0)) \in \mathcal{C}, \\ c'_0 &= G_0(w'_0) = (h_1(w'_0), \dots, h_n(w'_0)) \in \mathcal{C}, \end{aligned}$$

where all $c_t, c'_t \in \mathcal{C} \in \mathbb{R}^n$.

Employing Signum function $\text{sgn}(\cdot)$ for quantization, $h_i(\cdot)$ collectively provide a solution to the angle difference between (w_0, w'_0) , which can be described as

$$\begin{aligned} \theta_0 &= d_H(c_0, c'_0) / n \\ &= \frac{\sum_i \text{sgn}(h_i(w_0)) \neq \text{sgn}(h_i(w'_0))}{n} = \frac{\arccos(w_0 \cdot w'_0)}{\pi}. \end{aligned}$$

The Hamming distance, $x = d_H(c_0, c'_0)$, between two codewords c_0 and c'_0 is found to conform to a Binomial distribution, denoted as $\text{Bin}(n, \theta_0)$. This relationship can be formulated as:

$$\text{Pr}[x = k] = \binom{n}{k} (\theta_0)^k (1 - \theta_0)^{n-k}. \quad (11)$$

Owing to the Central Limit Theorem (CLT), when n is large, the Hamming distance $x = d_H(c_0, c'_0)$ can be normalized, taking the form $(d_H(c_0, c'_0) - n\theta_0) / \sqrt{n\theta_0(1 - \theta_0)}$, which tends to converge towards a standard normal distribution, $\mathcal{N}(0, 1)$. This observation implies that $d_H(c_0, c'_0)$ aligns closely with a normal distribution, precisely $\mathcal{N}(n\theta_0, n\theta_0(1 - \theta_0))$ when large enough n is in used. Given the *principle of maximum entropy*, the standard normal distribution, therefore, naturally serves as an optimal candidate for maximizing the entropy of the densities within our examination, supporting the model’s interpretability in harmony with the second law of thermodynamics, as outlined in Eq. 9.

Denoted a new set of measurements, termed “reduced codewords” as follows:

$$\begin{aligned}\hat{c}_1 &= \hat{G}_1(w_0) = (\hat{h}_1(w_0), \dots, \hat{h}_k(w_0)), \hat{c}_1 \in \mathbb{R}^k \\ \hat{c}'_1 &= \hat{G}_1(w'_0) = (\hat{h}_1(w'_0), \dots, \hat{h}_k(w'_0)), \hat{c}'_1 \in \mathbb{R}^k\end{aligned}$$

Each reduced codeword defined to be non-discrete ($\hat{c}_{t+1} \in \mathbb{R}^k$ and $\hat{c}'_{t+1} \in \mathbb{R}^k$) within a reduced dimensionality $k < n$ that aligns to their original sample (w_t, w'_t) in \mathbb{R}^k . These reduced codewords are derived from a subset, namely “reduced matrix”, $\hat{G}_{t+1} \subseteq G_t$ consisting of k hash functions drawn from the generator function G_t without any quantization. More specifically,

$$\hat{h}_i(w_0) = (v_i^T \cdot w_0) \in \mathbb{R}, \text{ for } i = 1, \dots, k.$$

To satisfy the necessary constraint established in Eq. 8, $f(x, k; \theta_1)$ should be expressed as a fraction, specifically $1/\binom{n}{k}$, of the true density $f(x, k; \theta_0)$. This implies that $f(x, k; \theta_1)$ represents a specified case, preferably the worst-case scenario, among the $\binom{n}{k}$ possible outcomes of the true density. We achieve this by maximize the “relative distance” between the reduced codeword \hat{c}_1 and c_1 as follows:

Let assume $w'_0 = 0^k$, it means $c'_0 = 0^n$ represents the null vector in the higher-dimensional space. Since $n > k$, we can establish a \mathbb{R}^{k+1} dimensional subspace. This subspace consists of k -dimension hyperplanes with $\hat{c}'_1 = 0^k$ serving as their origin. The reduced codeword \hat{c}_1 that is the furthest from $\hat{c}'_1 = 0^k$ can be identified by selecting the k largest absolute outputs from the original codeword c_0 , i.e., the Euclidean distance $d(\hat{c}_1, 0^k)$ is maximum. These outputs, in conjunction with their corresponding hash $\hat{h}_1, \dots, \hat{h}_k$ functions, form the reduced matrix \hat{G}_1 .

When the distance $d(\hat{c}_1, 0^k)$ is maximized, we effectively adhere to our previous formulation. This formulation aims to identify features $w_{t+1} = \hat{c}_{t+1}$ that have a low probability of occurrence (indicating they are non-robust) and are positioned farthest from $w'_{t+1} = \hat{c}'_{t+1} = 0^k$, which serves as the origin for each k -dimensional hyperplane as increasing t .

Decoding: Through cosine-distance based LSH, we can obtain a solution to the angle difference between any non zero w_0 and w'_0 by calculating the Hamming distance between \hat{c}_1 and \hat{c}'_1 . If one found the Hamming distance $d_H(\hat{c}_1, \hat{c}'_1) = k$, a solution must also exist for

$$\begin{aligned}\theta_1 &= d_H(\hat{c}_1, \hat{c}'_1)/n = \frac{\sum_i^k \text{sgn}(\hat{h}_i(w_0)) \neq \text{sgn}(\hat{h}_i(w'_0))}{n} \\ &= \frac{\arccos(w_0 \cdot w'_0)}{\pi} = k/n.\end{aligned}$$

Above derivation establishes the conclusion that $\theta_1 = \theta_0 = k/n$ with respect to the mean of the standard normal distribution (in accordance with the CLT for large n):

$$\begin{aligned}d_H(\hat{c}_1, \hat{c}'_1) - n\theta_1 &= d_H(c_0, c'_0) - n\theta_0 = 0 \\ \Rightarrow \theta_0 &= \theta_1 = k/n.\end{aligned}\quad (12)$$

Consequently, the densities corresponds to $\theta_0 = \theta$ can therefore have their ratio complies with Eq. 8.

With the described encoding process iterated repeatedly and independently, resulting new features $w_{t+1} = \hat{c}_{t+1}$ and $w'_{t+1} = \hat{c}'_{t+1}$ at each iteration t , Equation 12 can be expanded to include multiple parameters by undergoing continuous

encoding iterations up to a maximum encoding time step t , as follows:

$$\begin{aligned}d_H(\hat{c}_{t+1}, \hat{c}'_{t+1}) - n\theta_{t+1} &= \dots = d_H(c_0, c'_0) - n\theta_0 = 0 \\ \Rightarrow \theta_0 &= \theta_1 = \dots = \theta_{t+1} = k/n,\end{aligned}$$

thus satisfies the requirement in Eq. 9.

An Euclidean Spacetime Geometric Interpretation: To better visualize and understand this process, we adopt a geometrical interpretation, represented in Figure 1a. This illustration demonstrates the influence of three successive encoding stages: from $t = 0, 1, 2$. Although our model can easily extend to higher dimensions, including a \mathbb{R}^{k+1} subspace for arbitrary large n and $k < n$, for ease of visualization, we only focus on scenarios where $k = 2$, considering a 2-D space. In this context, the \mathbb{R}^{k+1} subspace contains maximum $t + 1$ unique hyperplanes (including initial condition $t = 0$). Each step at t corresponds to a new solution of $w'_{t+1} = 0^k$ describing its largest distance with w_{t+1} along the additional dimension—the temporal axis. Each new encoding introduces a fresh hyperplane, collectively giving rise to a 3-D spacetime representation.

Model’s Efficiency: Note that despite the fact that there is an exponential growth in entanglement complexity as delineated in Eq. 9, the intrinsic encoding and decoding process remains computationally efficient. Specifically, the resultant reduced codewords, (\hat{c}_{t+1} and \hat{c}'_{t+1}) at encoding time step t , manifest quadratic time computational complexity, denoted as $O(n^2t)$ (see Algorithm 1 and 2 for asymptotic large n). Figure 1b illustrates a toy example on how Algorithm 1 operates at $t = 0, 1, 2$ to produce reduced matrices $\{\hat{G}_1, \hat{G}_2, \hat{G}_3\}$ and their corresponding reduced codewords $\{\hat{c}_1, \hat{c}_2, \hat{c}_3\}$.

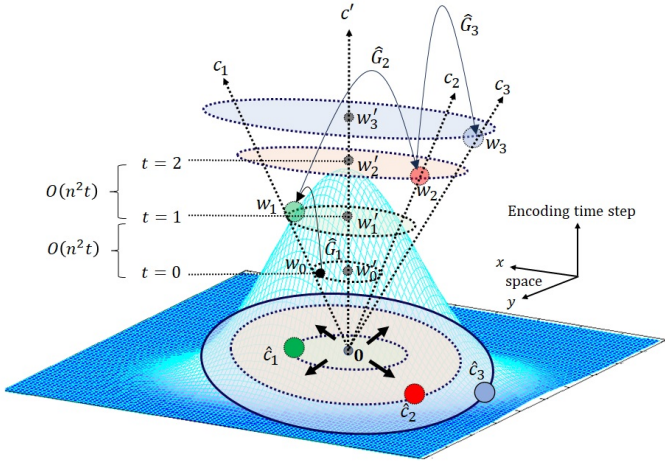
3.2 Model’s Completeness

Noting the equivalence $\hat{c}_{t+1} = w_{t+1}$ and $\hat{c}'_{t+1} = w'_{t+1}$, we conveniently substitute (w_t, w'_t) with (\hat{c}_t, \hat{c}'_t) for $t > 0$ in subsequent analyses, particularly when examining their Euclidean distance and angle difference. To ensure comprehensive information regarding the true densities of the evolving system, we extend our considerations to multi-parameter settings $(\theta_0, \dots, \theta_{t+1})$.

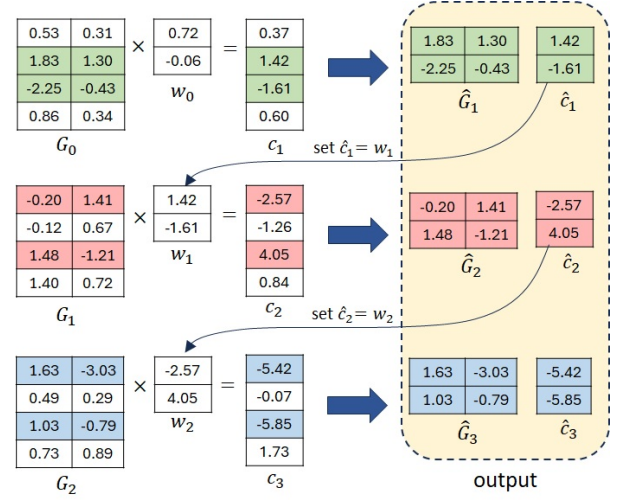
3.2.1 Introducing Computational Relativity

Drawing a parallel to the Einstein’s theory of special relativity [32], where all physical laws remain the same in every inertial reference frame, we treat w_t , and w'_t as distinct physical entities by their coordinate $w_t \in \mathbb{R}^k$ and $w'_t \in \mathbb{R}^k$.

Since each encoding time step ($t > 0$) can be made corresponds to specific time interval s_t , for instance $s_t = 1$ means one second; any solution for w_t deviates from w'_t with a maximum speed of $\frac{d(w_t, w'_t)}{s_t} \leq v_t$ is computationally feasible within our model. This inequality holds because of $d(w_t, w'_t)$ corresponds to maximum distance where their reduced codewords counterpart s.t. \hat{c}_t is furthest away from $\hat{c}'_t = 0^k$. This give us solution to the spacetime interval between two events always less than or equal to zero, as in $d(w_t, w'_t)^2 - (v_t s_t)^2 \leq 0$. This scenario holds significance in Minkowski’s spacetime diagram (see Figure 2). In particular, when we set v_t equal to the speed of light, events fall within



(a) Figure demonstrates the progressive divergence of w_t and w'_t , equivalent to their reduced codewords counterpart $(\hat{c}_{t+1}, \hat{c}'_{t+1})$ with increasing encoding time step. We employ subscript notation to indicate that the reduced matrix \hat{G}_{t+1} corresponds to arbitrary maximum encoding time steps $t = 0, t = 1$ and $t = 2$. For non-trivial encoding, w_0 should start from a non-zero value.



(b) Example ($n = 4, k = 2$) demonstrates the encoding process with $t = 0, t = 1$, and $t = 2$. This process can be repeated for arbitrary large t . Alternatively, one can view the overall encoding as an evolving function, represented by $f(x; y; t) = \hat{G}_{t+1} \hat{G}_t \dots \hat{G}_1(x; y) = w_{t+1} = \hat{c}_{t+1}$ treat $x = 0.72$ and $y = -0.06$ as an initial condition.

Fig. 1: Continuous encoding illustration for $t = 0, 1, 2$.

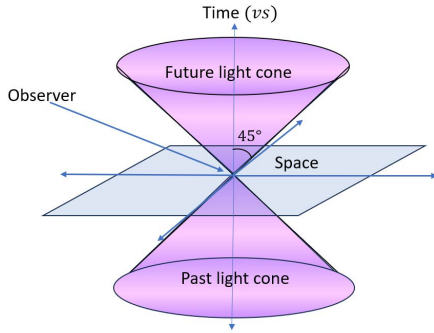


Fig. 2: The Minkowski's spacetime diagram. v is the speed of light and s is unit of time (second).

the “light cone” in Minkowski's spacetime diagram, known as the timelike region. This cone-shaped boundary with a maximum angle of $\theta\pi = 45^\circ$ defines the limits of causality and where information and physical effects can propagate.

Conversely, when $d(w_t, w'_t)^2 - (v_t s_t)^2 > 0$ is the case, marking the region beyond the light cone, it is denoted as the spacelike area. In this spacelike region, events find themselves entirely devoid of any conceivable causal connection to the origin. Thus, an event occurring in the spacelike region is causally disconnected from the origin. No signal, even one moving at the speed of light, could reach from the origin to the spacelike event (or vice versa) without surpassing the speed of light.

Taking Theory of Relativity as Physical Constraint: Building upon theory of relativity, we underscore a constraint that is necessarily to preserve the principle of causality within our model, which is

$$\theta_0\pi = \theta_1\pi = \dots = \theta_{t+1}\pi = k\pi/n \leq 45^\circ.$$

This constraint, where the maximum angle difference is set at 45° , imposes a minimum requirement on the codeword length n for arbitrary input dimensions k , ensuring alignment with the theory of relativity, specifically through the concept of the light cone. To uphold a constant angle difference in between (w_t, w'_t) across distinct hyperplanes, s.t. $\theta_0 = \theta_1 = \dots = \theta_{t+1} = k/n \leq 1/4$, n and k must be constant through the whole encoding process and also $k/n \leq 1/4$.

Nevertheless, as the encoding process continues with the previous reduced codeword as input, the distance $d(w_t, w'_t)$ will increase. Since the angle difference between (w_t, w'_t) can be well approximated using small angle approximation (means large n), follows:

$$\theta_t\pi = k\pi/n \approx \tan \theta_t\pi = d(w_t, w'_t)/s_t.$$

Consequently, for sufficiently large $t > 0$, the increases of $d(w_t, w'_t)$ may lead to $\theta_t\pi > 45^\circ$, thus violate the principle of causality. In such a case, the corresponding time intervals s_t must be dilated, i.e., from s_t to $s_{t'} > s_t$ and v_t must be reduced, i.e., from v_t to $v_{t'} < v_t$. This phenomenon is essential to preserve the invariance of the spacetime interval across all local frames of reference, corresponds to particular light cone, at various computational complexities, as follows:

$$d(w_t, w'_t)^2 - (v_t s_t)^2 = d(w_{t'}, w'_{t'})^2 - (v_{t'} s_{t'})^2 = 0, \quad (13)$$

with referring to a common origin 0, for $t = t' > 0$.

With above condition applied, we can consider the entire set of solutions $\{d(w_0, w'_0), d(w_1, w'_1), \dots, d(w_{t+1}, w'_{t+1})\}$ and $\{\theta_0\pi, \theta_1\pi, \dots, \theta_{t+1}\pi\}$ as a cohesive entity within an evolving system, jointly connected under a common origin at 0.

Time Dilation and Length Contraction

We borrow Figure 3 for more comprehensive illustration. Let take example to the case when $t = 0$, refer to the grey light cone (left most). Given that $v_{t=0} = d(w_0, w_0)/s_{t=0}$ corresponds to the maximum speed of light, the angle difference $\theta_0\pi = 45^\circ$ must be at its maximum. As t increases to $t = 1$, we shift our attention to the new light cone (in green) with $d(w_1, w'_1) > d(w_0, w_0)$. Since the green light cone must also correspond to the maximum speed of light $v_{t=1}$ at $t = 1$, the angle difference $\theta_1\pi = 45^\circ$. The only way to join these two light cones (grey and green) with respect to the same origin 0 is through the dilation of $s_{t=0}$ to $s_{t'=0}$, where the speed $v_{t'=0}$ will necessarily decrease to uphold spacetime interval invariance in accordance with Eq. 13 for the grey light cone at $t = t'$.

Computational Time Dilation: Let $d(w_{t'}, w'_{t'})^2 = (x_{t'})^2 + (y_{t'})^2$ with respect to $w'_{t'} = 0^k$ as the origin for $k = 2$ -dimensions of space. The most common form of the Lorentz transformation, utilized in theory of relativity, can be parametrized by $v_{t'}$ confined to the x -direction, expressed as:

$$\begin{aligned} s_t &= \gamma(s_{t'} - \frac{v_{t'}x_{t'}}{v_t^2}), \\ x_t &= \gamma(x_{t'} - v_{t'}s_{t'}), \\ y_t &= y_{t'}, \end{aligned}$$

with $\gamma = 1/\sqrt{1 - \frac{(v_{t'})^2}{v_t^2}}$ representing these Lorentz factor. Utilizing the Lorentz transformation equations, the changes of time interval ($\Delta s_t, \Delta s_{t'}$) measured within an inertial frame of reference, corresponds to a particular light cone at arbitrary encoding time steps $t = t' > 0$ therefore follows the time dilation formula:

$$\Delta s_t = \frac{\Delta s_{t'}}{\sqrt{1 - \frac{(v_{t'})^2}{v_t^2}}}. \quad (14)$$

Computational Length Contraction: The length contraction can be readily derived in similar way with given formula:

$$\Delta x_t = \Delta x_{t'} \sqrt{1 - \frac{(v_{t'})^2}{v_t^2}}. \quad (15)$$

This implies that any measured length ($\Delta s_t, \Delta s_{t'}$) within an inertial frame of reference appears contracted for a specific light cone at arbitrary encoding time steps $t = t' > 0$.

3.2.2 Experimental Validation of Computational Time Dilation and Length Contraction

Algorithm 1 and 2 outline the pseudocode for generating the entangled pairs \hat{c}_t and \hat{c}'_t , respectively, using the same set of reduced matrices $\{\hat{G}_1, \dots, \hat{G}_t\}$.

To validate the time dilation and length contraction effects we have derived, we adopted the MagFace model [33] to generate 6000 pairs of feature samples $(w_0, w'_0)_{6000}$ that possesses a dimensionality of $\ell = 512$. The datasets employed for this experiment is LFW [34]. Among these pairs, 3,000 were belongs to inter-class comparisons, such that $w_0^{(\text{inter})}$ is expected to be orthogonal to $w'_0^{(\text{inter})}$. Another 3000 pair were used for intra-class comparisons, where the angle between $w_0^{(\text{intra})}$ and $w'_0^{(\text{intra})}$ is expected less than 45° .

This design ensures that the inter-class pairs exhibit non-local correlation, i.e., over spacelike region within the light cone, in contrary to the intra-class pairs.

Evidence for Time Dilation: Figure 4 illustrates the Hamming distance $d_H(\hat{c}_t, \hat{c}'_t)$ and $\theta_t = \arccos(\hat{c}_t, \hat{c}'_t)/\pi$ computed between the generated reduced codewords \hat{c}_t and \hat{c}'_t for both inter and intra classes ($n = 2000, k = 500$). As t increases, the changes of the value θ_t tends to behave in one of two ways: it either converges to zero or one. The decrease in angle difference, converges to zero, is attributed to the expansion of spacetime. This is argued to be accompanied by time dilation, ensuring the invariance of spacetime intervals. Changing the sign of \hat{c}_t to $-\hat{c}_t$ can achieve convergence in reverse, leading to their angle difference maximized.

Evidence for Length Contraction: Taking into consideration on both perfect correlation, where $\hat{c}_t = \hat{c}'_t$ and perfect anti-correlation, where $\hat{c}_t = -\hat{c}'_t$ are possible, we computed the squared Enclidian distance between $(\hat{c}_t, -\hat{c}'_t)$ and (\hat{c}_t, \hat{c}'_t) . Figure 5 presents the computed squared Euclidean distances for both inter-class and intra-class comparisons ($n = 2000, k = 500$). As t increases, we observe contrasting convergence behaviors for inter-class and intra-class comparisons. Their distances either converge to zero (0) or four (4). The convergence to a distance of zero is evident when $\hat{c}_t = \hat{c}'_t$. On the other hand, the convergence to a distance of four can be explained by the triangle inequality $\|a - b\| \leq \|a\| + \|b\| \leq 2$. For $\hat{c}_t = -\hat{c}'_t$ opposite to each other, their squared Euclidean distance is at maximum four.

Figures 6 and 7 illustrate the continuous encoding process with maximum $t = 200$, resulting in perfect correlation and anti-correlation between (\hat{c}_t, \hat{c}'_t) and $(-\hat{c}_t, \hat{c}'_t)$ respectively. As the parameter n increases, the discernible patterns in the evolution of these reduced codewords become more pronounced, despite the inherently random and stochastic nature of the encoding process itself. Although the inherent non-local correlation exhibited by inter-class pairs, our findings highlight their susceptibility to becoming computationally entangled within our model as t increases.

4 INFORMATION RECONCILIATION VIA COMPUTATIONAL ENTANGLEMENT

Figure 8a illustrates an example of how computational entanglement can be applied to adopted which facilitates reliable information transmission through information reconciliation.

Information reconciliation [35]–[37] is a cryptographic method that ensures Alice and Bob share a common secret after exchanging data over an unreliable channel, rectifying any errors and inconsistencies.

In this context, we considered Alice and Bob, each independently sampling random features denoted as w_0 and w'_0 , respectively, following specific probability distributions, such as the standard normal distribution. Given the freedom to utilize an encoder associated with a collection of reduction matrices, denoted as $\{\hat{G}_1, \dots, \hat{G}_t\}$; with a sufficiently large t , Alice and Bob can collaboratively generate reduced codewords, \hat{c}_t and \hat{c}'_t , that possess perfect correlation or anti-correlation through computational entanglement. These entangled codewords can subsequently serve as a means for encoding and decoding a message denoted as m , thus

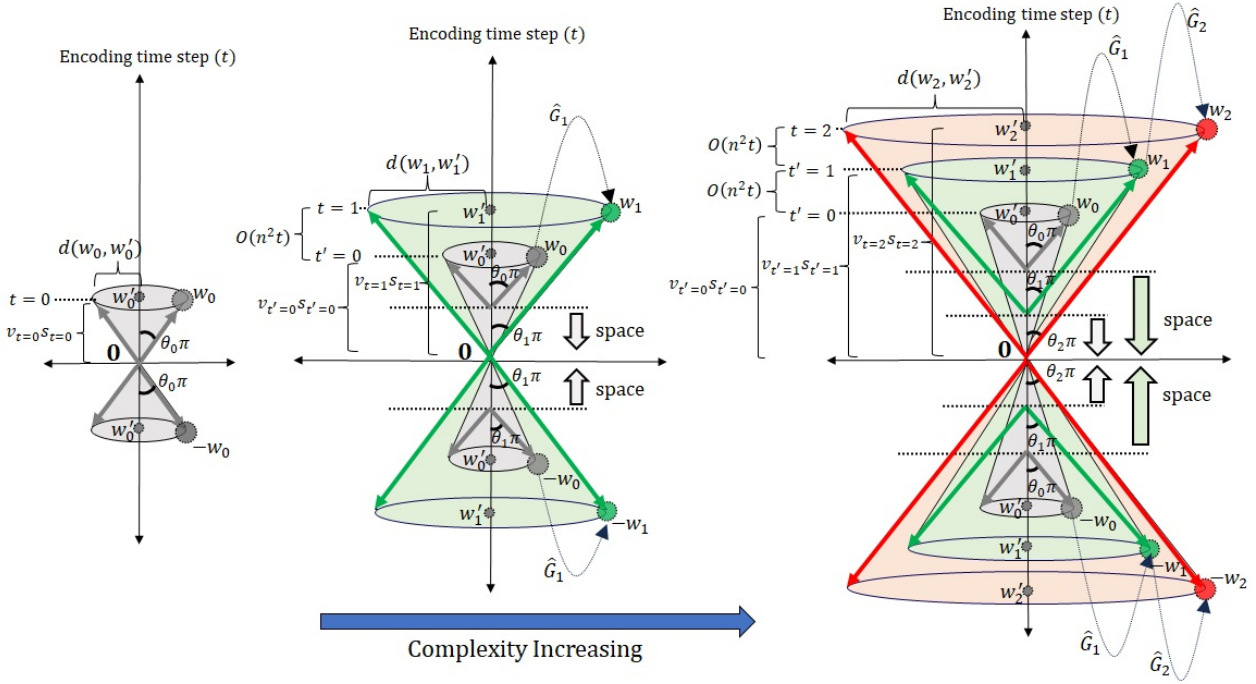


Fig. 3: When referring to a fixed w'_t , there are two types of correlation: either $+\cos\theta_t\pi = w'_t \cdot w_t$ or $-\cos\theta_t\pi = w'_t \cdot -w_t$ (anti-correlation). This give rise to symmetrical light cone structure. Each colored arrow pointing to w_t represents its direction, with an angle of $\theta_t\pi$ rotating around the axis of encoding time step. When these vectors share a common origin (e.g., at point 0), the angle between them in various local frames of reference (represented by grey, green, and red cones) increases over time. To uphold $\theta_0\pi = \theta_1\pi = \dots = \theta_t\pi$, spacetime must expand and the time interval s_t dilated to $s_{t'}$. Such dilation results in a decrease in the angle between $(w_{t'}, w'_t)$ and $(-w_t, w'_t)$ within a specific light cone, referring to the common origin 0.

Algorithm 1 Algorithm 1

- 1: **function** Encode(w_0, n, t)
 - 2: Sample $G \leftarrow \mathbb{R}^{n \times \ell}$ \triangleright where ℓ is the dimension of w
 - 3: Compute $c = Gw_0$
 - 4: Compute $\hat{c} \leftarrow c$ and $\hat{G} \leftarrow G$
 - 5: Normalize $\hat{c} = \hat{c}/\|\hat{c}\|$
 - 6: Record \hat{c} and \hat{G}
 - 7: Set $w_0 = \hat{c}$, and repeat Step 2 to Step 6 for t iterations.
 - 8: **Output** $\{\hat{c}_1 \dots, \hat{c}_t\}$ and $\{\hat{G}_1 \dots, \hat{G}_t\}$ \triangleright Equivalently, we can treat $\{\hat{c}_1 \dots, \hat{c}_t\}$ as $\{w_1 \dots, w_t\}$.
 - 9: **end function**
-

Algorithm 2 Algorithm 2

- 1: **function** Project($\{\hat{G}_1 \dots, \hat{G}_t\}, w'_0$)
 - 2: **for** $i = 1 : t$ **do**
 - 3: Compute $\hat{c}'_i = \hat{G}_i w'_0$
 - 4: Set $\hat{c}_i = \hat{c}'_i / \|\hat{c}'_i\|$ \triangleright Normalization take place here
 - 5: Record \hat{c}_i
 - 6: Set $w'_0 = \hat{c}'_i$
 - 7: **end for**
 - 8: **Output** $\{\hat{c}'_1 \dots, \hat{c}'_t\}$ \triangleright Equivalently, we can treat $\{\hat{c}'_1 \dots, \hat{c}'_t\}$ as $\{w'_1 \dots, w'_t\}$.
 - 9: **end function**
-

facilitating information transmission between the parties involved. This implies that any encoded message, denoted as

$$y = \text{sgn}(\hat{c}_t) + m,$$

is recoverable through the decoding process, follows

$$y - \text{sgn}(\hat{c}'_t) = (\text{sgn}(\hat{c}_t) - \text{sgn}(\hat{c}'_t)) + m,$$

leading to the recovered output to be either equal to m or $1^k - m$. Since, in principle, the entangled codewords can demonstrate a normalized Hamming distance converged to either zero or one.

Achieving Computational Security through Computational Entanglement: In the context of secure communication, it's crucial to acknowledge that the encoded message is

susceptible to eavesdropping or malicious tampering by an active adversary. Therefore, the selection of the maximum encoding time step, (t) , should align with the minimum requirement for Bob to decode the message effectively using the set of reduced matrices $\{\hat{G}_1, \dots, \hat{G}_t\}$.

More specifically, any adversary can, with a sufficiently large value of t , sample an arbitrary random $w_0^* \in \mathbb{R}^k$ result in the creation of reduced codewords \hat{c}_t^* that will also entangled with \hat{c}_t (provided that the knowledge of the reduced matrices $\{\hat{G}_1, \dots, \hat{G}_t\}$ is available). Subsequently, these entangled codewords have the capability to accurately decode the message hence compromised the system security.

In the light of above, the establishment of secure commu-

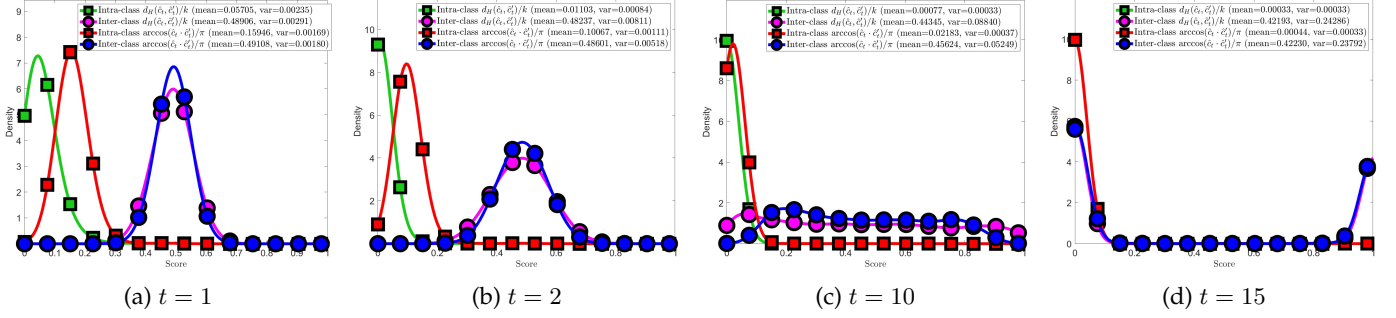


Fig. 4: Result for time dilation validation.

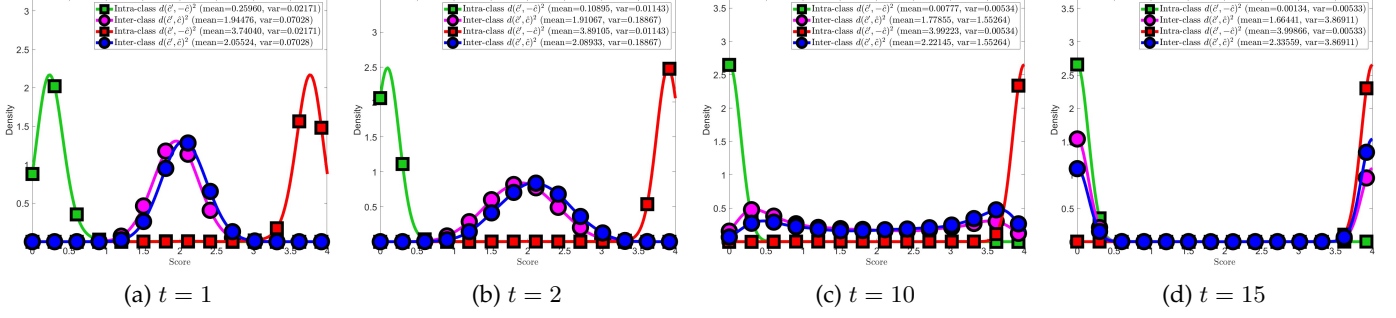
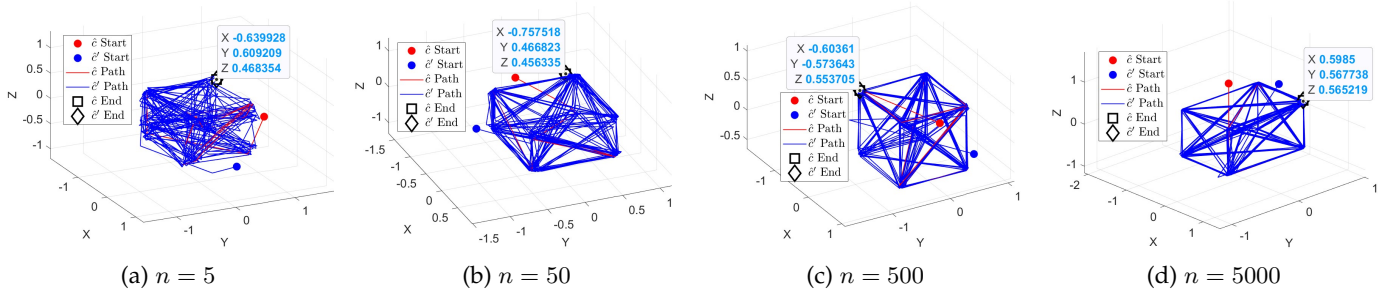
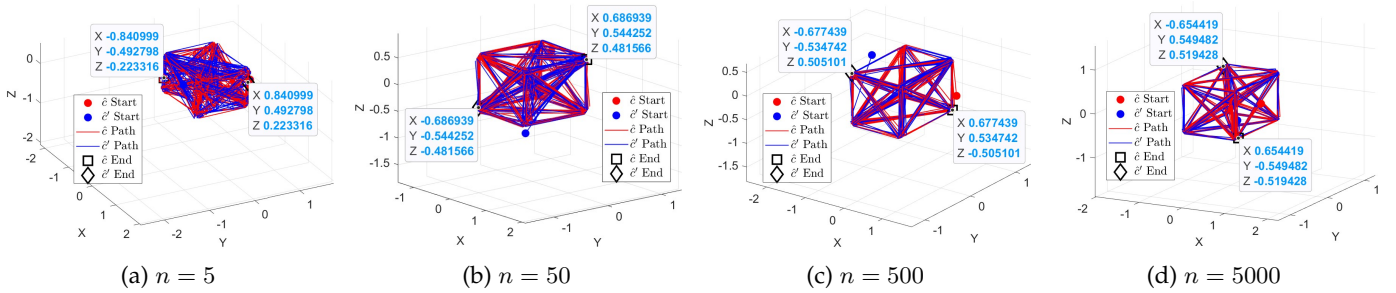


Fig. 5: Result for length contraction validation.

Fig. 6: Perfect correlation scenarios at $k = 3$ -dimensionFig. 7: Perfect anti-correlation scenarios at $k = 3$ -dimension

nication channel, while acknowledging the potential of computational entanglement, essentially relies on the requirement that *only Alice and Bob* have the capacity to establish computational entangled correlation over their respective sample pair (w_0, w'_0) in an efficient manner. This capability sets them apart from potential adversaries, granting them a significant advantage. In a more appropriate context, Alice and Bob can pre-shared the reduced matrices $\{\hat{G}_1, \dots, \hat{G}_t\}$ necessary to generate an entangled reduced codeword pair (\hat{c}_t, \hat{c}'_t) . Without access to the knowledge of $\{\hat{G}_1, \dots, \hat{G}_t\}$, any potential adversary would have no guarantee of establishing a causal relationship with \hat{c}_t through computational

entanglement and would lack the ability to efficiently decode the message from y using arbitrary random sample w_0^* . This phenomenon gives rise to a decoding problem for the adversary, linked to the decoding of random linear codes, which has been established as an NP-hard problem [38].

4.0.1 A Case Study

Figure 8b illustrates the outcomes of our practical application of computational entanglement for encoding arbitrary messages, represented as 50×50 (equivalently vector representation of $k = 2500$) binary images encompassing various objects like dogs, laptops, airplanes, crosses, and fish. The process involves the generation of reduced codeword pairs

(\hat{c}_t, \hat{c}'_t) from feature samples (w_0, w'_0) , which are randomly drawn from a standard normal distribution. The encoded message appears initially as random and noisy.

As t increases, the entanglement process unfolds, leading to the emergence of relativistic effects such as time dilation and length contraction. The system entropy then continues to decrease. These effects ultimately entangle every bit of the reduced codeword pair (\hat{c}_t, \hat{c}'_t) , enabling the successful decoding of the message using \hat{c}'_t through the operation $y - \hat{c}'_t$, resulting in a perfect recovery of the original message.

4.1 Adversary Example Generation Through the Lens of Information Reconciliation

In continuation of our earlier discussion regarding information reconciliation, we now embark on a deeper examination, shedding light on how this process can be harnessed to facilitate the generation of adversarial examples as depicted in Figure 9a.

In this scenario, an adversary can create an adversarial example by injecting random noise into an ‘‘Panda’’ sample (m), represented as $y = \alpha \hat{c}_t + m$, where w is random noise following a standard normal distribution, and \hat{c}_t is a reduced codeword generated from w with arbitrary variance controlled by α .

Our findings reveal the possibility of generating a reduced codeword, \hat{c}'_t , from a random sample referred to as ‘‘Gibbon’’ (w'), which is computationally entangled with \hat{c}_t . This entangled codeword pair (\hat{c}_t, \hat{c}'_t) is the key to effectively reconcile ‘‘Panda’’ information from the adversarial example y , even when the ‘‘Gibbon’’ sample initially appears unrelated or uncorrelated to ‘‘Panda’’.

As part of our assessment, we employed images of ‘‘Gibbon’’ and ‘‘Panda,’’ each sized at 50×50 , and chose $n = k + 1000$ to expedite the attainment of a fully entangled state. In Figure 9b, we observe the impact of increasing α on the original sample, resulting in the generation of the adversary example y . It becomes evident that higher levels of noise necessitate a greater number of iterations to successfully reconcile the original ‘‘Panda’’ sample from y , utilizing the ‘‘Gibbon’’ sample. What’s crucial to emphasize here is that our results demonstrate a significant insight: *human-imperceptible adversarial examples could essentially represent a specialized case of information reconciliation, particularly when the noise level is low.*

5 CONCLUSIVE STATEMENT

Within this discourse, we have put forth a computational interpretation of the emergence of adversarial examples in machine learning by delving into the concept of computational entanglement and relativity. By shedding light on relativistic effects such as time dilation and length contraction, previously overlooked in this context, we broaden our understanding of the intricacies involved. The intriguing prospect of entanglement even when feature samples are widely separated prompts a call for intensified research efforts to unravel the extent to which established machine learning models align with fundamental principles of physics.

It is imperative to approach the pursuit of model accuracy with caution, particularly when opting for increasingly complex and less interpretable models. Our research

unequivocally reveals the presence of computational entanglement, which can be effectively established in a linear fashion. This discovery strongly suggests that even highly complex models, such as deep neural networks with intricate layer connections, may be susceptible to the derived time dilation and length contraction effects, owing to their inherent piecewise linearity. These effects can lead to distinct features exhibiting perfect correlation or anti-correlation, making them susceptible to the emergence of adversarial examples.

DATA AVAILABILITY

The datasets generated and/or analyzed in the course of this study can be accessed on GitHub at the following link: [Link Here](#).

REFERENCES

- [1] T. B. Brown, N. Carlini, C. Zhang, C. Olsson, P. Christiano, and I. Goodfellow, ‘‘Unrestricted adversarial examples,’’ *arXiv preprint arXiv:1809.08352*, 2018.
- [2] I. J. Goodfellow, J. Shlens, and C. Szegedy, ‘‘Explaining and harnessing adversarial examples,’’ *arXiv preprint arXiv:1412.6572*, 2014.
- [3] C. Xiao, J.-Y. Zhu, B. Li, W. He, M. Liu, and D. Song, ‘‘Spatially transformed adversarial examples,’’ *arXiv preprint arXiv:1801.02612*, 2018.
- [4] S. Baluja and I. Fischer, ‘‘Adversarial transformation networks: Learning to generate adversarial examples,’’ *arXiv preprint arXiv:1703.09387*, 2017.
- [5] C. Xiao, B. Li, J.-Y. Zhu, W. He, M. Liu, and D. Song, ‘‘Generating adversarial examples with adversarial networks,’’ *arXiv preprint arXiv:1801.02610*, 2018.
- [6] K. F. Hossain, S. A. Kamran, A. Tavakkoli, L. Pan, X. Ma, S. Rajasegarar, and C. Karmaker, ‘‘Ecg-adv-gan: Detecting ecg adversarial examples with conditional generative adversarial networks,’’ in *2021 20th IEEE International Conference on Machine Learning and Applications (ICMLA)*. IEEE, 2021, pp. 50–56.
- [7] X. Chen, X. Gao, J. Zhao, K. Ye, and C.-Z. Xu, ‘‘Advdiffuser: Natural adversarial example synthesis with diffusion models,’’ in *Proceedings of the IEEE/CVF International Conference on Computer Vision*, 2023, pp. 4562–4572.
- [8] J. Gilmer, L. Metz, F. Faghri, S. S. Schoenholz, M. Raghu, M. Wattenberg, and I. Goodfellow, ‘‘Adversarial spheres,’’ *arXiv preprint arXiv:1801.02774*, 2018.
- [9] S. Bubeck, Y. T. Lee, E. Price, and I. Razenshteyn, ‘‘Adversarial examples from computational constraints,’’ in *International Conference on Machine Learning*. PMLR, 2019, pp. 831–840.
- [10] A. Shafahi, W. R. Huang, C. Studer, S. Feizi, and T. Goldstein, ‘‘Are adversarial examples inevitable?’’ *arXiv preprint arXiv:1809.02104*, 2018.
- [11] A. Madry, A. Makelov, L. Schmidt, D. Tsipras, and A. Vladu, ‘‘Towards deep learning models resistant to adversarial attacks,’’ *arXiv preprint arXiv:1706.06083*, 2017.
- [12] D. Stutz, M. Hein, and B. Schiele, ‘‘Disentangling adversarial robustness and generalization,’’ in *Proceedings of the IEEE/CVF Conference on Computer Vision and Pattern Recognition*, 2019, pp. 6976–6987.
- [13] A. Ilyas, S. Santurkar, D. Tsipras, L. Engstrom, B. Tran, and A. Madry, ‘‘Adversarial examples are not bugs, they are features,’’ *Advances in neural information processing systems*, vol. 32, 2019.
- [14] P. Nakkiran, ‘‘A discussion of adversarial examples are not bugs, they are features’: Adversarial examples are just bugs, too,’’ *Distill*, vol. 4, no. 8, pp. e00019–5, 2019.
- [15] E. Wallace, ‘‘A discussion of adversarial examples are not bugs, they are features’: Learning from incorrectly labeled data,’’ *Distill*, vol. 4, no. 8, pp. e00019–6, 2019.
- [16] I. Evtimov, I. C. Covert, A. Kusupati, and T. Kohno, ‘‘Disrupting model training with adversarial shortcuts,’’ in *ICML 2021 Workshop on Adversarial Machine Learning*, 2021.
- [17] A. Li, Y. Wang, Y. Guo, and Y. Wang, ‘‘Adversarial examples are not real features,’’ *arXiv preprint arXiv:2310.18936*, 2023.

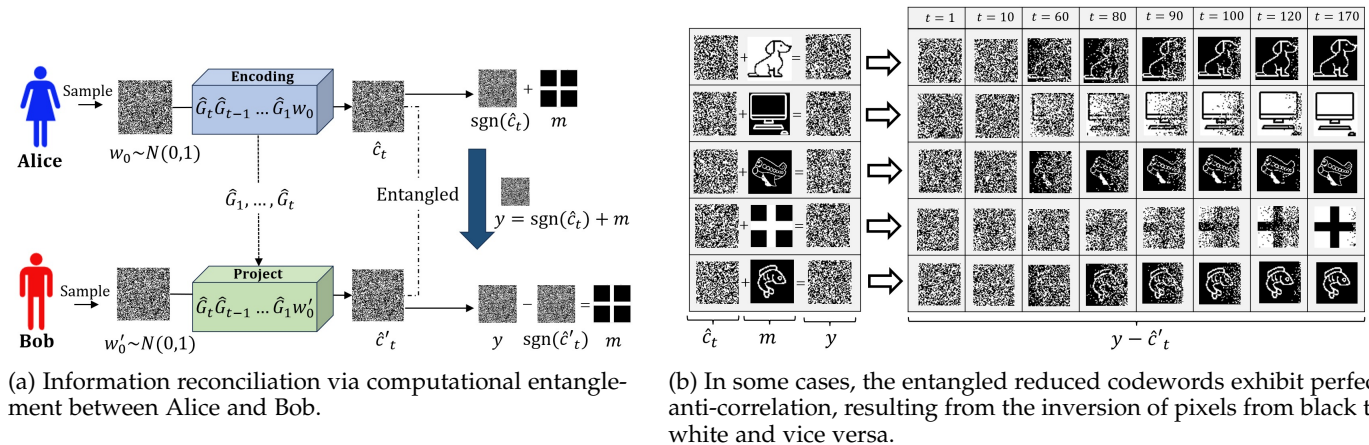


Fig. 8: Case study for information reconciliation with binary images.

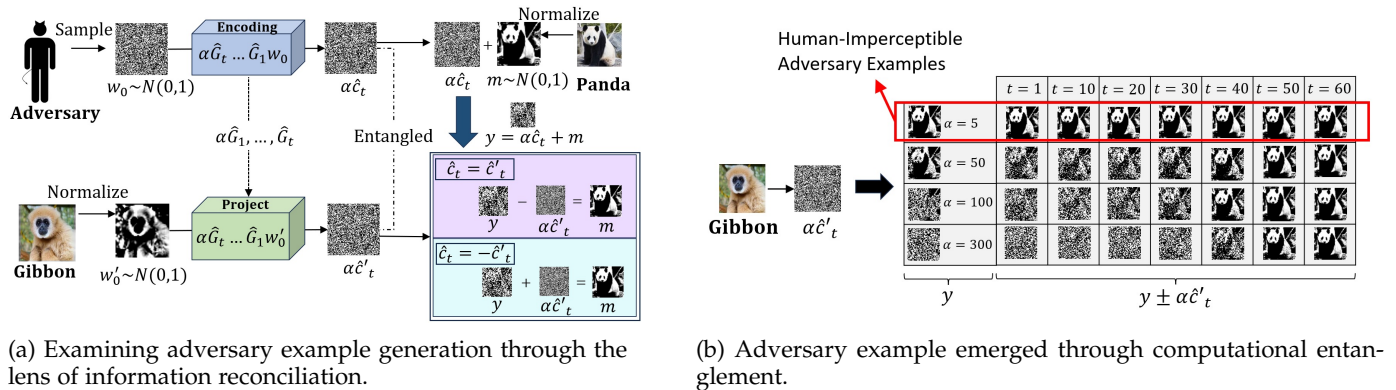


Fig. 9: Case study for emergence of adversary example through information reconciliation.

- [18] C. Buckner, "Understanding adversarial examples requires a theory of artefacts for deep learning," *Nature Machine Intelligence*, vol. 2, no. 12, pp. 731–736, 2020.
- [19] F. Waseda, S. Nishikawa, T.-N. Le, H. H. Nguyen, and I. Echizen, "Closer look at the transferability of adversarial examples: How they fool different models differently," in *Proceedings of the IEEE/CVF Winter Conference on Applications of Computer Vision*, 2023, pp. 1360–1368.
- [20] H. Zhang, D. Yu, Y. Lu, and D. He, "Adversarial noises are linearly separable for (nearly) random neural networks," in *International Conference on Artificial Intelligence and Statistics*. PMLR, 2023, pp. 2792–2804.
- [21] P. Benz, C. Zhang, and I. S. Kweon, "Batch normalization increases adversarial vulnerability and decreases adversarial transferability: A non-robust feature perspective," in *Proceedings of the IEEE/CVF International Conference on Computer Vision*, 2021, pp. 7818–7827.
- [22] S.-M. Moosavi-Dezfooli, A. Fawzi, J. Uesato, and P. Frossard, "Robustness via curvature regularization, and vice versa," in *Proceedings of the IEEE/CVF Conference on Computer Vision and Pattern Recognition*, 2019, pp. 9078–9086.
- [23] T. Tanay and L. Griffin, "A boundary tilting perspective on the phenomenon of adversarial examples," *arXiv preprint arXiv:1608.07690*, 2016.
- [24] A. Shamir, I. Safran, E. Ronen, and O. Dunkelman, "A simple explanation for the existence of adversarial examples with small hamming distance," *arXiv preprint arXiv:1901.10861*, 2019.
- [25] A. Shamir, O. Melamed, and O. BenShmuel, "The dimpled manifold model of adversarial examples in machine learning," *arXiv preprint arXiv:2106.10151*, 2021.
- [26] D. Warde-Farley, "1 adversarial perturbations of deep neural networks," 2016. [Online]. Available: <https://api.semanticscholar.org/CorpusID:28912221>
- [27] E. Berlekamp, *Algebraic coding theory*. World Scientific, 1968.
- [28] B. Biggio and F. Roli, *Adversarial Machine Learning*. Springer, 2018.
- [29] N. Inkawhich, W. Wen, and H. H. Liu, "Understanding and enhancing the transferability of adversarial examples," *arXiv preprint arXiv:2007.03256*, 2020.
- [30] A. R. Brown and L. Susskind, "Second law of quantum complexity," *Physical Review D*, vol. 97, no. 8, p. 086015, 2018.
- [31] M. S. Charikar, "Similarity estimation techniques from rounding algorithms," in *Proceedings of the thirty-fourth annual ACM symposium on Theory of computing*, 2002, pp. 380–388.
- [32] A. Einstein et al., "On the electrodynamics of moving bodies," *Annalen der physik*, vol. 17, no. 10, pp. 891–921, 1905.
- [33] Q. Meng, S. Zhao, Z. Huang, and F. Zhou, "Magface: A universal representation for face recognition and quality assessment," in *Proceedings of the IEEE/CVF Conference on Computer Vision and Pattern Recognition*, 2021, pp. 14 225–14 234.
- [34] G. B. Huang, M. Mattar, T. Berg, and E. Learned-Miller, "Labeled faces in the wild: A database for studying face recognition in unconstrained environments," in *Workshop on faces in 'Real-Life' Images: detection, alignment, and recognition*, 2008.
- [35] C. H. Bennett, G. Brassard, and J.-M. Robert, "Privacy amplification by public discussion," *SIAM journal on Computing*, vol. 17, no. 2, pp. 210–229, 1988.
- [36] S. Abruzzo, H. Kampermann, M. Mertz, and D. Bruß, "Quantum key distribution with finite resources: Secret key rates via rényi entropies," *Physical Review A*, vol. 84, no. 3, p. 032321, 2011.
- [37] R. Renner and S. Wolf, "Simple and tight bounds for information reconciliation and privacy amplification," in *International Conference on the Theory and Application of Cryptology and Information Security*. Springer, 2005, pp. 199–216.
- [38] E. Berlekamp, R. McEliece, and H. Van Tilborg, "On the inherent intractability of certain coding problems (corresp.)," *IEEE Transactions on Information Theory*, vol. 24, no. 3, pp. 384–386, 1978.

DERIVATION

Derivation of the Invariance of Spacetime Interval (Eq. 13)

Through referring to the identical colored light cone at encoding time step $t = t' > 0$, as illustrated in Figure 3, we can distinguish its *past* corresponds to the encoding time step t , while its *present* aligns with $t' = t$ at higher complexity level. When considers $w_{t'} = 0^k$ and $w'_t = 0^k$, the Euclidean distance between $d(w_t, w'_t)$ and $d(w_{t'}, w'_{t'})$ can be expressed as.

$$\begin{aligned} d(w_{t'}, w'_{t'})^2 &= x_{t'}^2 + y_{t'}^2, \\ d(w_t, w'_t)^2 &= x_t^2 + y_t^2. \end{aligned}$$

The Lorentz transformation relating the present light cone for $w_{t'}$ moving at reduced speed of light v'_t away from $w'_{t'} = 0^k$, with its motion confined solely in the x -direction across a two-dimensional space (x and y), can be described using equations:

$$\begin{aligned} s_t &= \gamma(s_{t'} - \frac{v_{t'} x_{t'}}{v_t^2}), \\ x_t &= \gamma(x_{t'} - v_{t'} s_{t'}), \\ y_t &= y_{t'}, \end{aligned}$$

The spacetime interval for the past light cone at encoding time step $t = t' > 0$, after applying the aforementioned transformation, proceeds as follows:

$$\begin{aligned} &d(w_t, w'_t)^2 - v_t^2 s_t^2 \\ &= x_t^2 + y_t^2 - v_t^2 s_t^2 \\ &= \gamma^2(x_{t'} - v_{t'} s_{t'})^2 + y_{t'}^2 - v_t^2 \gamma^2(s_{t'} - \frac{v_{t'} x_{t'}}{v_t^2})^2 \\ &= \gamma^2(x_{t'} - v_{t'} s_{t'})^2 + y_{t'}^2 - v_t^2 \gamma^2(s_{t'} - \frac{v_{t'} x_{t'}}{v_t^2})^2 \\ &= \frac{v_t^2}{v_t^2 - v_{t'}^2} \left(x_{t'}^2 - 2x_{t'} v_{t'} s_{t'} + v_{t'}^2 s_{t'}^2 \right) + y_{t'}^2 - \frac{v_t^2 \cdot v_{t'}^2}{v_t^2 - v_{t'}^2} \left(s_{t'}^2 - 2s_{t'} \frac{v_{t'} x_{t'}}{v_t^2} + \frac{v_{t'}^2 x_{t'}^2}{v_t^4} \right) \\ &= \frac{v_t^2}{v_t^2 - v_{t'}^2} \left[x_{t'}^2 - 2x_{t'} v_{t'} s_{t'} + v_{t'}^2 s_{t'}^2 - v_t^2 s_{t'}^2 + 2s_{t'} v_{t'} x_{t'} - \frac{v_{t'}^2 x_{t'}^2}{v_t^2} \right] + y_{t'}^2 \\ &= \frac{v_t^2}{v_t^2 - v_{t'}^2} \left[\frac{x_{t'}^2}{v_t^2} (v_t^2 - v_{t'}^2) - s_{t'}^2 (v_t^2 - v_{t'}^2) \right] + y_{t'}^2 \\ &= x_{t'}^2 + y_{t'}^2 - v_{t'}^2 s_{t'}^2 \\ &= d(w_{t'}, w'_{t'})^2 - v_{t'}^2 s_{t'}^2 \\ &\Rightarrow d(w_t, w'_t)^2 - v_t^2 s_t^2 = d(w_{t'}, w'_{t'})^2 - v_{t'}^2 s_{t'}^2. \end{aligned}$$

Since for identical light cone but different encoding time step t and $t' = t > 0$, the computed distance $d(w_t, w'_t) = d(w_{t'}, w'_{t'})$ remain the same. Due to the time interval $s_{t'}$ is dilated, the last line of above equation necessitates a reduces in v_t to $v_{t'} < v_t$ to uphold its invariance under Lorentz transformation.

Since $d(w_t, w'_t)^2 - v_t^2 s_t^2 = 0$ (as we taking v_t as the speed of light, with maximum $\theta_0 \pi = 45^\circ$ to uphold the principle of causality), it means:

$$d(w_t, w'_t)^2 - v_t^2 s_t^2 = d(w_{t'}, w'_{t'})^2 - v_{t'}^2 s_{t'}^2 = 0$$

Derivation of Time Dilation (Eq. 14)

We can apply Lorentz transformation for the time s_t at encoding time step $t = t' > 0$ measured in distinct events A and B described as equations below:

$$\begin{aligned} s_t^{(A)} &= \gamma(s_{t'}^{(A)} - \frac{v_{t'} x_{t'}^{(A)}}{v_t^2}), \\ s_t^{(B)} &= \gamma(s_{t'}^{(B)} - \frac{v_{t'} x_{t'}^{(B)}}{v_t^2}). \end{aligned}$$

The difference of the time interval between these two events simply equal to their differences:

$$\begin{aligned} s_t^{(A)} - s_t^{(B)} &= \gamma(s_{t'}^{(A)} - \frac{v_{t'} x_{t'}^{(A)}}{v_t^2}) - \gamma(s_{t'}^{(B)} - \frac{v_{t'} x_{t'}^{(B)}}{v_t^2}) \\ &= \gamma(s_{t'}^{(A)} - s_{t'}^{(B)} - \frac{v_{t'}}{v_t^2} (x_{t'}^{(A)} - x_{t'}^{(B)})) \\ &\Rightarrow \Delta s_t = \gamma(\Delta s_{t'} - \frac{v_{t'}}{v_t^2} \Delta x_{t'}) \end{aligned} \tag{16}$$

Since we only focus on particular light cone at encoding time step $t = t' > 0$, its computed distance $d(w_{t'}, w'_t) = d(w_t, w'_t)$ always remain constant thus the change in distance over x -direction, $\Delta x_{t'}$, will be zero. This lead us to conclude:

$$\Delta s_t = \frac{\Delta s_{t'}}{\sqrt{1 - \frac{v_{t'}^2}{v_t^2}}},$$

where the time interval measured in reference frame of higher complexity level for a particular light cone at previous encoding time step $t = t' > 0$ must be dilated follows above equation.

Derivation of Length Contraction (Eq. 15)

We can utilize the Lorentz transformation to compute the length, which is equivalent to the Euclidean distance restricted to the x -direction between w_t and w'_t . The length in any two events A and B at encoding time step $t = t' > 0$ described as equations below:

$$\begin{aligned} x_t^{(A)} &= \gamma(x_{t'}^{(A)} - v_{t'} s_{t'}^{(A)}), \\ x_t^{(B)} &= \gamma(x_{t'}^{(B)} - v_{t'} s_{t'}^{(B)}). \end{aligned}$$

The changes in the length measured between these two events are:

$$\begin{aligned} x_t^{(A)} - x_t^{(B)} &= \gamma(x_{t'}^{(A)} - v_{t'} s_{t'}^{(A)}) - \gamma(x_{t'}^{(B)} - v_{t'} s_{t'}^{(B)}) \\ &= \gamma((x_{t'}^{(A)} - x_{t'}^{(B)}) - v_{t'}(s_{t'}^{(A)} - s_{t'}^{(B)})) \\ &\Rightarrow \Delta x_t = \gamma(\Delta x_{t'} - v_{t'} \Delta s_{t'}). \end{aligned} \quad (17)$$

Focusing solely on a particular light cone at the encoding time step $t = t'$, any valid changes in the length Δx_t within a moment of time must indicate $s_t^{(A)} = s_t^{(B)}$. Noting that above time interval $\Delta s_{t'}$ is at encoding time step t' rather than t , therefore we need to refer to the equation obtained during derivation of time dilation formula (Eq. 16):

$$s_t^{(A)} - s_t^{(B)} = \gamma(s_{t'}^{(A)} - \frac{v_{t'} x_{t'}^{(A)}}{v_t^2}) - \gamma(s_{t'}^{(B)} - \frac{v_{t'} x_{t'}^{(B)}}{v_t^2}).$$

For $s_t^{(A)} = s_t^{(B)}$:

$$\begin{aligned} 0 &= \gamma(s_{t'}^{(A)} - s_{t'}^{(B)} - \frac{v_{t'}}{v_t^2}(x_{t'}^{(A)} - x_{t'}^{(B)})) \\ &\Rightarrow s_{t'}^{(A)} - s_{t'}^{(B)} = \Delta s_{t'} = \frac{v_{t'}}{v_t^2}(x_{t'}^{(A)} - x_{t'}^{(B)}). \end{aligned} \quad (18)$$

Substitute Eq. 18 to Eq. 17:

$$\begin{aligned} \Delta x_t &= \gamma(\Delta x_{t'} - \frac{v_{t'}^2}{v_t^2} \Delta x_{t'}) \\ &= \gamma \Delta x_{t'} \left(1 - \frac{v_{t'}^2}{v_t^2}\right) = \frac{\Delta x_{t'}}{\gamma} \\ &\Rightarrow \Delta x_t = \Delta x_{t'} \sqrt{1 - \frac{v_{t'}^2}{v_t^2}}. \end{aligned}$$

Above result leads us to conclude that any changes in the length Δx_t of a specific light cone at previous encoding time step $t = t' > 0$ will appear to be contracted at higher complexity level of encoding time step $t' = t > 0$.